IOP Publishing Journal of Physics: Condensed Matter
J. Phys.: Condens. Matter **34** (2022) 255002 (11pp) https://doi.org/10.1088/1361-648X/ac62a3

Modeling surface spin polarization on ceria-supported Pt nanoparticles

Byungkyun Kang[1], Joshua L Vincent[2], Yongbin Lee[3], Liqin Ke[3], Peter A Crozier[2] and Qiang Zhu[1,*]

[1] Department of Physics and Astronomy, University of Nevada, Las Vegas, NV 89154, United States of America
[2] School for Engineering of Matter, Transport, and Energy, Arizona State University, Tempe, AZ 85281, United States of America
[3] Ames Laboratory, US Department of Energy, Ames, IA 50011, United States of America

E-mail: qiang.zhu@unlv.edu

Received 29 January 2022, revised 15 March 2022
Accepted for publication 30 March 2022
Published 22 April 2022

Abstract

In this work, we employ density functional theory simulations to investigate possible spin polarization of CeO_2-(111) surface and its impact on the interactions between a ceria support and Pt nanoparticles. With a Gaussian type orbital basis, our simulations suggest that the CeO_2-(111) surface exhibits a robust surface spin polarization due to the internal charge transfer between atomic Ce and O layers. In turn, it can lower the surface oxygen vacancy formation energy and enhance the oxide reducibility. We show that the inclusion of spin polarization can significantly reduce the major activation barrier in the proposed reaction pathway of CO oxidation on ceria-supported Pt nanoparticles. For metal-support interactions, surface spin polarization enhances the bonding between Pt nanoparticles and ceria surface oxygen, while CO adsorption on Pt nanoparticles weakens the interfacial interaction regardless of spin polarization. However, the stable surface spin polarization can only be found in the simulations based on the Gaussian type orbital basis. Given the potential importance in the design of future high-performance catalysts, our present study suggests a pressing need to examine the surface ferromagnetism of transition metal oxides in both experiment and theory.

Keywords: first-principles calculation, spin polarization, surfaces

(Some figures may appear in colour only in the online journal)

1. Introduction

In heterogeneous catalysis, metal nanoparticles supported on reducible oxide structures provide unique interfacial interactions, which lead to the formation of active sites at the three-phase boundaries, controlling activity and selectivity for oxidation reactions [1, 2]. Many high-performance heterogeneous catalysts have been developed by exploiting the metal/oxide interface properties for reactions such as CO oxidation at room and low temperatures [3–6]. The ability of reducible oxides to donate lattice oxygen during a reaction (the so-called Mars van Krevellen mechanism) was first described nearly 70 years ago and is now an accepted kinetic pathway for many reactions [7]. The atomic-level details of how such a mechanism operates, especially in the presence of metallic nanoparticles, remain poorly understood. Tauster was one of the first to recognize the unique properties of the metal-support interaction (MSI) with his observation of metal nanoparticles being encapsulated with thin overlayers under strong reducing conditions [8–10]. The strong MSI has been realized in redox transition metal oxides [8–11] and even a relatively redox-inert alkaline metal oxide MgO [12]. The MSI is also associated with the occurrence of charge transfer at the interface [13]. Campbell proposed the electronic MSI mechanism, in which charge transfer at the metal/oxide interface modulates the chemical activity of the supported catalyst [14]. The electronic MSI gives rise to a rearrangement of electrons

* Author to whom any correspondence should be addressed.

within the interface and enhances the rate of surface oxygen vacancy creation/annihilation, leading to an enhanced catalytic activity [15].

To manipulate the role of the interfacial interactions on a catalytic reaction, one can vary nanoparticles' size to change the contact area between the metal and support interface [16]. For example, for Au/Co_3O_4 and Au/Fe_2O_3, the gold nanoparticles with a diameter smaller than 5 nm showed high reaction activity [17], while Pt nanoparticles of 2–3 nm were found to be more active for CO oxidation [18]. In the limiting case, the metal nanoparticles may be reduced all the way down to a single atom, giving rise to the so-called single-atom catalysts [19]. Another approach to manipulate catalytic activity is by tuning the interfacial interaction directly. This has been realized by varying the support type, particles shape and size. The aforementioned nanostructuring creates new MSI resulting in the metal nanoparticle properties being substantially different from their bulk counterparts [16]. Doping oxides by heteroatoms can modify the electronic structure. They enhance surface oxygen reducibility by tuning the interfacial interaction [20]. The increased oxide reducibility linked to surface oxygen vacancy formation energy is an indispensable element in oxidation reactions based on the Mars–van Krevelen mechanism [20–25]. In combination with the smaller nanoparticles, nano-structured oxide supports further lower the formation energy of surface oxygen vacancy and give rise to a reverse spillover of the surface oxygen onto the Pt nanoparticle [26]. These works highlight the importance of undertaking fundamental studies to elucidate the complex interfacial interaction underlying catalytic functionality.

There remains a paucity of information about the atomic structure and the structural dynamics of an active metal-support interface performing catalysis. Recently, there has been an emerging paradigm that has roots in surface science [27–29] and chemistry [30] for understanding catalytically active sites in terms of dynamic, meta-stable, or so-called fluxional species from both computation [31–33] and experimental work [34–36]. This has raised many questions regarding both the fundamental structure of active sites and the atomic scale evolution of the interface, metal particle, and adjacent oxide surface during catalysis. For example, what is the dynamic nature of the metal-support interface? The adhesion between the metal particle and support may weaken significantly since bridging oxygen are responsible for anchoring the metal to the support. How does the metal-support interface change in the presence of reactant adsorbates and reaction intermediates? How do such structural changes impact the activation of intermediates and facilitate the bond breaking and formation along the reaction pathways? What happens during the rate-limiting step, and where is the likely site for CO_2 formation and desorption? In order to deepen our understanding of the factors affecting catalysis and to develop strategies for improved catalyst design, it is essential to elucidate and describe the structural evolution that occurs at the atomic level during simultaneous catalytic turnover.

In this work, we investigated the interfacial interaction of ceria-supported Pt nanoparticles by density functional theory (DFT) simulations. We found that spins are polarized on the CeO_2-(111) surface through charge transfer from surface oxygen to cerium, which can significantly lower the oxygen vacancy formation energy and alter the interfacial interaction between Pt nanoparticle and ceria support. In turn, the activated surface plays an essential role in lowering the major activation barrier in the proposed reaction pathway of CO oxidation on the ceria-supported Pt nanoparticles. Using the existence of a robust surface spin polarization, we propose a theoretical description of the recently observed controversial room temperature magnetism in ceria nanostructures [37]. Our modeling of surface spin polarization on bare ceria surface is also applicable in the fields of band gap opening, spintronics and thermoelectricity of 2D magnetic materials [38–40]. Particularly, electronic structure of surface spin polarized CeO_2 is akin to 2D ferromagnetic insulator [41, 42], where doping can allow spin-polarized current [43–45]. We found the surface spin polarization is only stabilized in DFT simulation with a Gaussian type orbital basis. However, the presence of surface spin polarization cannot be validated by DFT simulations based on the plane wave methods. The detailed comparison based on different simulation methods is presented at the end of this paper.

2. Computational methods

We used the slab model with five O–Ce–O layers to simulate the CeO_2-(111) surface with a 6×6 reconstruction of the primitive unit cell. Experimental lattice constants ($a = b =$ 5.410 Å) [46] of ceria with 15 Å vacuum along the z direction have been used throughout. To make Pt-(111) interface with CeO_2-(111), a hexagonal Pt_{19} single layer (SL) was built. As initial structure for geometry optimization, we have located the center of Pt_{19} SL 2.5 Å above oxygen on the CeO_2-(111) surface, while Pt_{19} SL [100] and CeO_2 [110] are coincided. This model was relaxed at the level of DFT by using the CP2K package [47]. The distance between Pt and surface Ce are around 3.0 Å in relaxed structure, which is close to corresponding distance in HRTEM image in the author's paper [36]. In CP2K, the wavefunction was expanded in the double ζ valence plus polarization and plane-wave basis sets with an energy cutoff of 400 Ry. We used Geodecker–Teter–Hutter pseudopotentials [48] based on the GGA [49] functional. To account for dispersion interaction, the third-generation (D3) van der Waals correction [50] was adopted for all simulations. We note that our simulations for ceria slab with/without D3 correction show no change in the magnitude of surface spin polarization. For all spin polarized calculations, half spin moments on Pt and Ce atoms were given as the initial guess. To account for the strongly correlated nature of Ce's $4f$ electrons, we employed the DFT + U method with $U = 7$ eV, as suggested by the previous studies [51, 52]. To check the effect of U, we also repeated some representative calculations using $U = 4$ eV. The climbing image-nudged elastic band (CI-NEB) method [53] was used to simulate the activation barriers for the proposed reaction pathway of CO oxidation on the ceria-supported Pt nanoparticles. To find surface spin polarization effect on the lattice dynamic reconfiguration, we performed the *ab-initio* molecular dynamic (AIMD) simulation at 300 K with 1 fs time

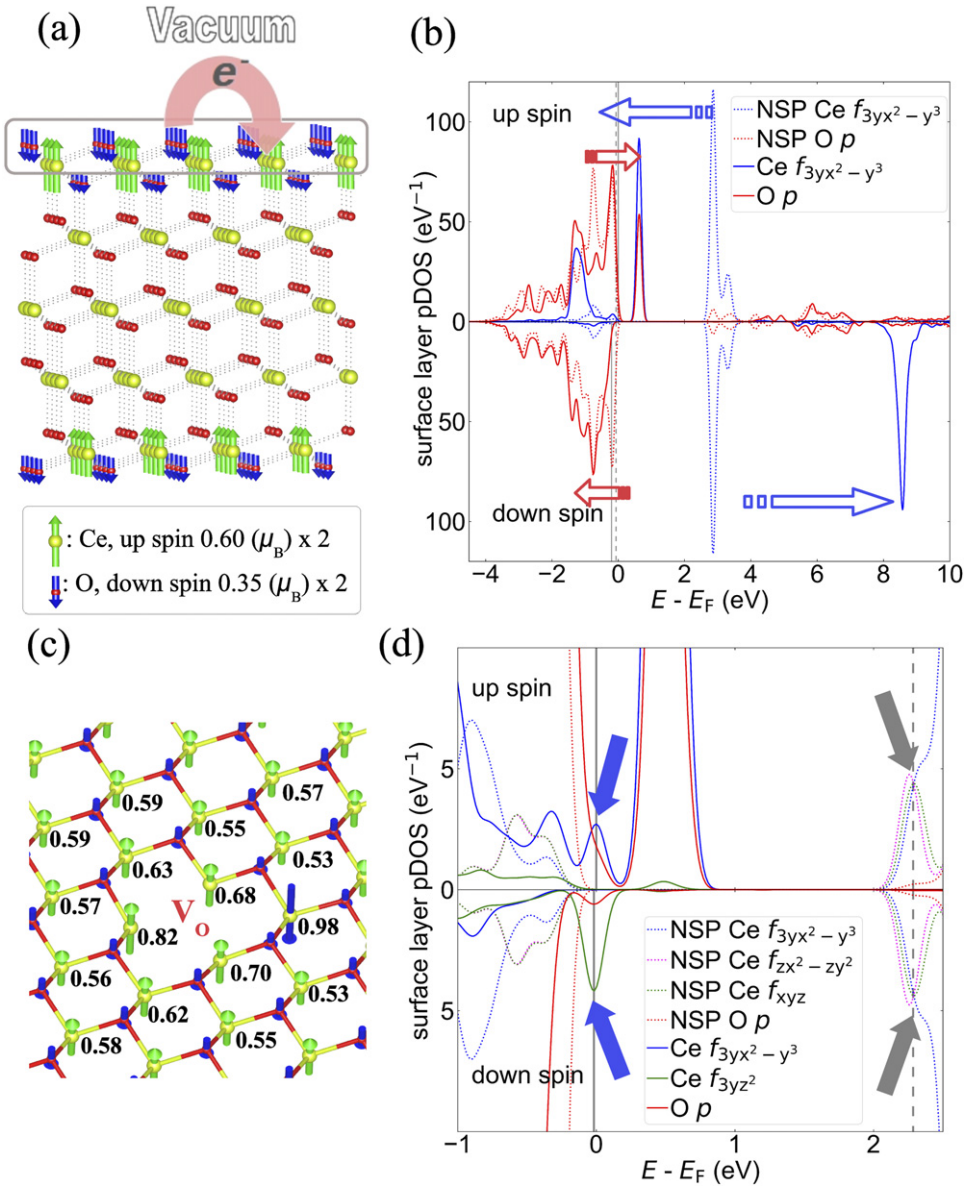

Figure 1. Calculated surface spin polarization and surface oxygen vacancy. (a) Optimized CeO_2-(111) surface. Green (blue) vector denotes calculated Mulliken up (down) spin population multiplied by scale factor 2.0 for visualizing the moment (note that the same scale factor is used for all figures in this work). For clarity, only the spin population larger than 0.20 μ_B is shown here. The lower inset shows the scale of vectors. (b) Calculated surface layer projected density of state. The density of state of upper oxygen and cerium layers marked by gray box in (a) are shown. The blue (red) arrows denote the relative shifts of Ce-f (O-p) states between SP and NSP simulations. (c) Optimized surface geometry with oxygen vacancy. (d) Calculated surface layer projected density of state for the oxygen vacancy configuration. The blue (gray) arrows point to defect states obtained from SP (NSP) simulation. In (c) and (d), the zero of energy set to chemical potential of up spin from spin polarized simulation, and relative chemical potentials are marked by solid (dashed) vertical lines for SP (NSP) simulation.

step using Nose–Hoover thermostat. To prevent high computational cost, only three layers of O–Ce–O were considered in the AIMD simulation. In all simulations, the atoms on the lowest O–Ce–O layer were kept fixed.

From the aforementioned DFT simulations, we obtained the adsorption energy using the following equation:

$$E_{ads} = E_{(slab\_adsorbate)} - E_{slab} - E_{adsorbate} \quad (1)$$

where $E_{(slab\_adsorbate)}$ is the energy of optimized slab model with adsorbates, E_{slab} is the energy of pure surface slab, and $E_{adsorbate}$ is the energy of adsorbate, respectively.

Oxygen vacancy formation energy is

$$E^F_{Vo} = E_{(slab\_Vo)} - E_{slab} + 1/2E_{O_2} \quad (2)$$

where E_{O_2} is the total energy of the ground (triplet) state of oxygen molecule in the gas phase.

Surface energy of slab is defined by

$$E_{surf} = (E_{slab} - nE_{bulk})/(2S) \quad (3)$$

where n is the number of formula unit in the slab, and S is the surface area.

3. Result and discussions

3.1. Surface spin polarization

We first performed the geometry optimization with initial magnetic moment on all cerium atoms to include surface spin polarization explicitly. Figure 1(a) shows the optimized CeO_2-(111) surface where spins are polarized. The average Mulliken spin moment per atom is 0.60 (-0.35) μ_B on the uppermost cerium (oxygen) layer. This structure contains spin polarization on both top and bottom O–Ce–O surface layers. The spin polarization in the bottom layer (with frozen atoms) is weaker than that in the upper layer (with free atoms). Figure 1(b) shows the projected density of states (DOS) of surface layers. For a comparison, the DOS without spin polarization is also shown here. The spin polarized DOS near the Fermi energy is comprised of appreciable hybridization between Ce-f and O-p orbitals. The occupied (unoccupied) up spin states derived by bonding (antibonding) of Ce-f and O-p characters form the narrow bands. The exchange splitting is explained by a comprehensive comparison of spin polarized (SP) and non-spin polarized (NSP) DOS. Compared to the NSP system, the Ce-f states were split into the unoccupied down spin states and occupied up spin states (see the blue arrows in figure 1(b)). In consequence, the net up spin moment is populated on surface cerium atoms. On the other hand, the original O-p states (from NSP calculation) were pushed up into unoccupied state in up spin and pushed down into lower energy states in down spin (see the red arrows in figure 1(b)), resulting a population of the net down spin moment on surface oxygen atoms.

Compared to the NSP calculation, the inclusion of spin polarization lowers the total energy by 7.83 eV. The energy drop is derived by just outermost two O–Ce–O layers (surface layers) where spins are polarized, since there is no sizable spin polarization on other layers. Accordingly, the energy gain corresponds to 3.92 eV per surface layer or 0.11 eV per O–Ce–O in the surface layer (there are 36 O–Ce–O units in the surface layer). One can confirm that this estimation is appropriate based on constant total energy difference between SP and NSP systems with respect to number of layers, as shown in table 1. This significant energy difference indicates the existence of a strong spin polarization on CeO_2-(111) surface. We did not find any antiferromagnetic configuration in this system. Therefore, we conclude that the CeO_2-(111) surface is ferromagnetic. Although the calculated total spin moments in the SP system is zero, the magnetic moment of an atom increases not only with spin moment but also with angular moment. Thus, the spin moment of the Ce atom dominates the field polarization upon magnetic field applied, leading to a ferromagnetic or ferrimagnetic system.

While the room temperature magnetism in CeO_2 has been studied extensively, its origin remains unclear [37]. Here, we propose a new theoretical description of the room temperature ferromagnetism in undoped ceria nanostructure [54–60] and thin films [61–65]. It was suggested that the ferromagnetism is confined to the ceria nanostructure surface where oxygen vacancy may play an important role [57, 58, 61]. On the contrary, Li *et al* [55] and Liu *et al* [59] proposed that the ferromagnetism does not relate to the surface oxygen vacancy but to the surface Ce^{3+}/Ce^{4+} pairs. A number of DFT studies have attributed the ferromagnetism to native defects such as oxygen vacancy. The defect formation causes spin polarization of f electrons for Ce ions near the vacancy, resulting in a nonzero net magnetic moment on the ceria surface [63, 66–71]. Nevertheless, based on our results, the ferromagnetism may emerge in a bare surface without any defect or impurity. In general, it was perceived that ions on the surface with lower coordination numbers can cause an unusual spin population [72–74]. In our case, vacuum acts as a virtual doping on the surface: hole doping for oxygen layer lowering the chemical potential of surface oxygen and electron doping for cerium layer. Upon significant spin exchange interaction on the surface, the virtual doping leads to a charge transfer from oxygen layer to cerium layer, resulting in $Ce^{4+} \rightarrow Ce^{3+}$ transition and partially filled O-p on the surface layer (see figures 1(a) and (b)). In consequence, the spin on ions couples ferromagnetically, which gains significant energy comparing to the NSP system. In addition, we emphasize that the charge transfer is fully triggered by the surface effect. As shown in table 1, increasing the number of layers reduces the surface/bulk ratio, resulting in an increased chemical potential which approaches to that of the bulk, while other quantities show no sizable variation.

On account of the robust surface spin coupling, we investigated the impact of surface spin polarization on surface oxygen vacancy formation. Figure 1 shows the optimized structure, spin population and DOS of surface layer with oxygen vacancy. In the SP simulation, the two excess electrons produced by the oxygen vacancy are populated on neighboring cerium atoms forming localized polaronic states. One electron was captured by mostly one neighboring Ce atom, with the spin moments of 0.82 μ_B. The other electron was localized on the next nearest neighboring Ce atom with 0.98 μ_B down spin moment having antiferromagnetic coupling with the surrounding Ce atoms (see figure 2(a)). The latter is associated with the increased local spin moment by Hund's rule within our singlet simulation. The oxygen vacancy defect states in the SP system are shallow, whereas the same defect states are below conduction band minimum in the NSP system. With this configuration, we found the lowest surface oxygen vacancy formation energy is 0.38 eV in the surface spin polarized system. In contrast, the NSP simulations show higher oxygen vacancy formation energy values: 4.06 eV ($U = 7$ eV) and 3.04 eV ($U = 4$ eV), as compared to several previous reports ranged from 2.13 to 3.20 eV [60, 76–78]. Note that two electrons are almost equally populated on two nearest neighbor Ce atoms and one next nearest neighbor Ce in our NSP simulation. In the SP system, the less ionized oxygen ions bond weakly with cerium ions, resulting in lower cost of vacancy formation in comparison to the NSP system which does not involve charge transfer process. Therefore, our results indicate that surface spin polarization can lower the oxygen vacancy formation energy, and enhance the oxide reducibility of the CeO_2-(111) surface.

Table 1. The slab size effect on surface spin polarization. The O1 (O2) denotes oxygen atoms on the top (bottom) layer within the surface O–Ce–O layer. The calculated quantities by surface spin polarized (SP) and non-spin polarized (NSP) simulations are presented. E_{surf} is the calculated surface energy. E_F^{bulk} and E_F^{slab} are the Fermi energies for ceria bulk and slab, respectively. E_{SP} and E_{NSP} are total energies of SP and NSP systems, respectively. $\{O–Ce–O\}_{surf}$ denotes O–Ce–O in the surface layer.

		Number of O–Ce–O layers				
		3	5	7	9	11
Mulliken spin population in surface layer (μ_B/atom)	Ce	0.55	0.60	0.58	0.56	0.56
	O1	−0.32	−0.35	−0.34	−0.33	−0.33
	O2	−0.19	−0.20	−0.20	−0.20	−0.20
E_{surf} (J m^{-2})[a]	SP	0.94	0.94	0.95	0.95	0.96
	NSP	1.07	1.08	1.08	1.08	1.08
$E_F^{bulk} - E_F^{slab}$ (eV)	SP	8.34	6.86	5.59	4.70	4.04
	NSP	8.44	6.93	5.64	4.77	4.12
E_{SP}–E_{NSP} (eV/$\{O–Ce–O\}_{surf}$)		−0.11	−0.11	−0.10	−0.10	−0.10

[a]Experimental surface energy is 1.2 ± 0.2 J m^{-2} [75].

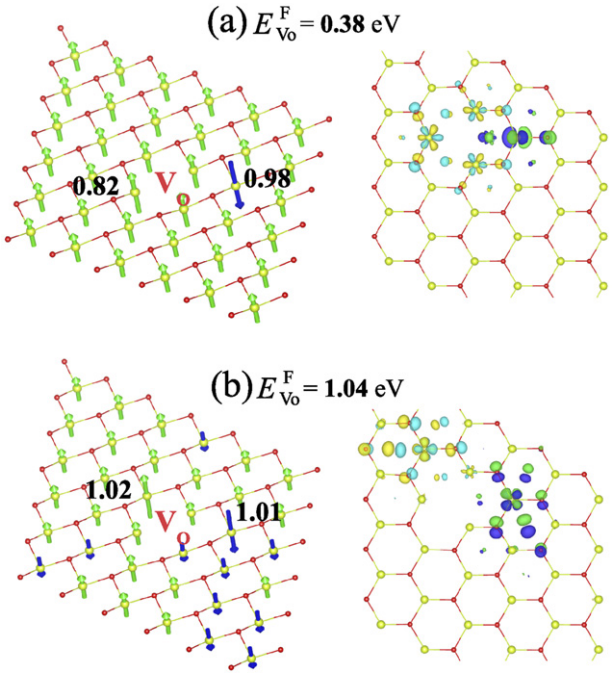

Figure 2. The calculated Mulliken up (down) spin population (left) and wavefunction isosurface of (0.05 e/Å^3) of the localized defect states, right) of two low-energy oxygen vacancy structures. (a) Shows the ground state configuration and (b) shows a representative metastable structure. The up (down) spin population (μ_B) is denoted by green (blue) vector. The yellow/cyan (green/blue) in the isosurface plot corresponds to positive/negative wavefunction of spin up (down) defect state.

In addition, we found another low-energy spin configuration (figure 2(b)) with two excess electrons being localized on the 2nd nearest neighbor Ce atoms. A similar configuration has been reported as the most stable configuration in other DFT studies [76, 77, 79]. However, it is no longer the ground state by considering the spin effect.

3.2. Pt on the ceria support with CO

To date, surface spin polarization has not been taken into account for nano-structured heterogeneous catalysts. Hence we investigated the influence of surface spin polarization on the interaction between Pt nanoparticle and ceria. As shown in figure 3(a), the optimized Pt_{19} SL on CeO_2-(111) consisted of platinum and surface oxygen (O_{surf}) bonds mostly on perimeter of the SL in NSP simulation. On the other hand, the SP simulation (see figure 3(c)) generates a configuration with more Pt–O_{surf} bonds. In addition, the averaged bond length is also shorter than that of the NSP configuration. This indicates that the interaction between ceria surface and Pt_{19} SL is significantly enhanced by the surface spin polarization. We attribute the strong Pt–O_{surf} bonds to electron depletion oxygen layer by the charge transfer on the spin polarized surface, where Pt atoms are more prone to oxidation. The enhanced interfacial interaction induces spin moments on Pt and Ce atoms and coupling between them. The surface oxygens were pulled out from ceria surface by this interaction. As a result, the donation of Pt valence electrons to surface oxygens increases the unpaired electron density around the Pt site. The pronounced on-site spin populations on Pt atoms are denoted in figure 3(c). The interfacial interaction also affects the electronic configuration of Ce atoms on the surface layer. The less oxidized Ce atoms have a large unpaired electron density which couples with the polarized Pt spins through surface oxygen. The majority of magnetic coupling is antiferromagnetic, resulting in a zero net spin moment on the intermediate surface oxygen.

Our simulation shows that adsorption energy of CO on the spin polarized CeO_2-(111) surface is −0.31 eV. The result agrees with previous observations that CO on CeO_2-(111) surface is either unstable or has weak interaction with the surface [80–82]. In terms of CO's adsorption energy on the ceria-supported Pt nanoparticle, our calculation reveals a wide distribution from −3.14 to −1.02 eV, depending on the choice of adsorption sites (data not shown). These results indicate that CO molecules are strongly adsorbed on Pt nanoparticles [83]. In this work, we constructed ceria-supported Pt_{19} SL with 12 CO molecules which were initially located at the bridging sites of the perimeter of Pt_{19}. Optimized geometries of $Pt_{19}[CO]_{12}$ with/without surface spin polarization are shown

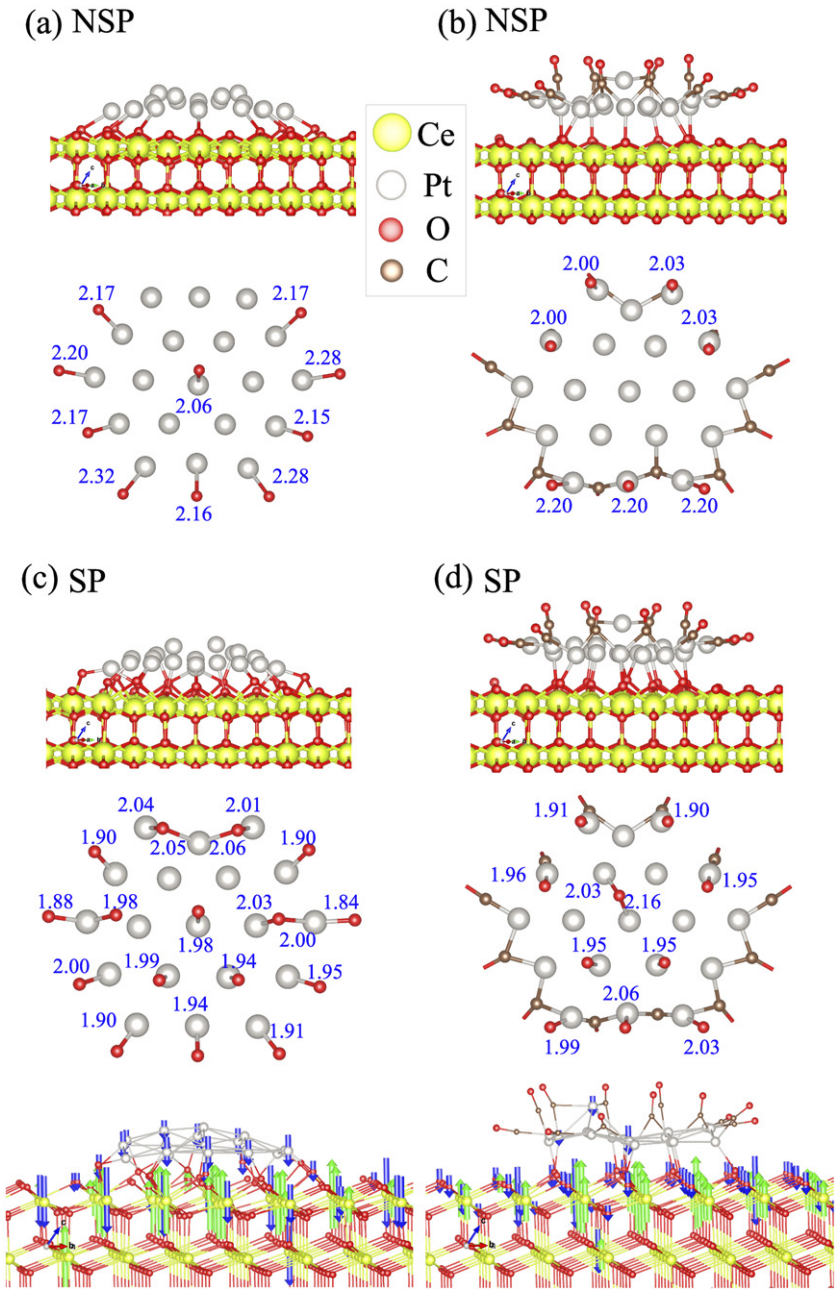

Figure 3. Optimized Pt single layer on ceria. (a) Pt_{19} single layer on a non-spin polarized CeO_2-(111) surface. (b) $Pt_{19}[CO]_{12}$ on a non-spin polarized CeO_2-(111) surface. (c) Pt_{19} single layer on a spin polarized CeO_2-(111) surface. (d) $Pt_{19}[CO]_{12}$ on a spin polarized CeO_2-(111) surface. The side view of the structures are shown in the top panel. The calculated bond lengths (Å) between Pt and surface oxygen are shown in the middle panel.

in figures 3(b) and (d). We again observed that surface spin polarization enhances the interaction between $Pt_{19}[CO]_{12}$ and ceria, i.e., more bonds and shorter bond lengths.

Figure 3 shows that the CO adsorption on Pt_{19} breaks a few $Pt–O_{surf}$ bonds on the perimeter of Pt_{19} in both NSP and SP calculations. Thus, the adsorption weakens the interfacial interaction. The weakening can be understood from Mulliken spin population analysis in the SP system. The strong CO adsorption on Pt_{19}, due to the π-back bonding between Pt and CO [84], can reduce the donation of Pt's valence electron to surface oxygen. As a result, the pairing electrons on Pt atoms decreases the net spin moment on the Pt_{19} (see figures 3(c) and (d)).

3.3. Reaction pathway in CO oxidation

We found that surface spin polarization may play an important role in the catalytic activity. On a spin polarized surface, the electrophilic oxygens in the electron deficient condition are more reactive with other species in comparison to the NSP system. In addition, new species formed by the reaction are easily removable owing to the high reducibility on the spin polarized surface. The impact of spin polarization on surface catalytic

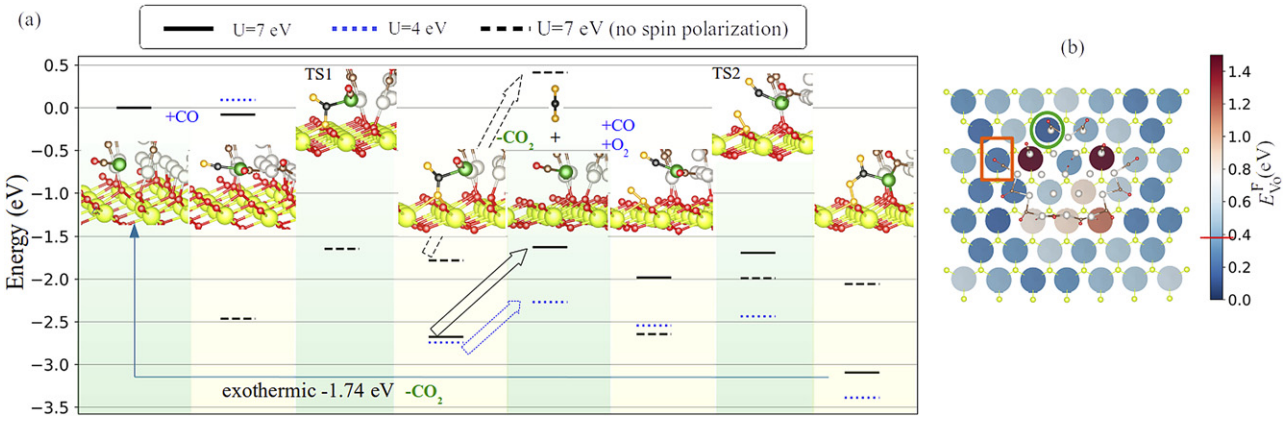

Figure 4. (a) The calculated energy profiles (shown as solid/dotted lines) for proposed reaction pathway for CO oxidation on $Pt_{19}[CO]_{11}$ with the ceria support. TS1 and TS2 denote two transition states. C(O) atoms involved in the reaction were colored in black (yellow), and the bonded Pt atoms are colored in green. (b) Calculated surface oxygen vacancy formation energies (shown as filled circles). The surface oxygen which react with CO was marked by the red box. The surface oxygen with exceptional low vacancy formation energy was marked by the green open circle. The energy level of oxygen vacancy formation for the most stable configuration on bare ceria surface is marked by red line on the energy color bar.

activity is illustrated in figure 4(a). We started with a CO desorpted $Pt_{19}[CO]_{11}$ with ceria support in CO rich conditions. The $Pt_{19}[CO]_{11}$ can adsorb one more CO molecule to form $Pt_{19}[CO]_{12}$, with a shallow adsorption energy of −0.08 eV. The adsorbed CO reacts with O_{surf} to form CO_2, gaining an energy of 2.60 eV. While there is no activation barrier for the reaction in the SP system, the calculated activation barrier is 0.82 eV in the NSP system. Taking off the CO_2 molecule from the reaction site leaves a surface oxygen vacancy, costing an penalty energy of 1.05 eV for $U = 7$ eV (0.47 eV for $U = 4$ eV). This is the main barrier in the proposed reaction pathway. The Pt SL can subsequently adsorb another incoming CO, while the ceria surface can attract O_2 at the oxygen vacancy site. The molecular O_2 and CO further react to form a new CO_2. The calculated activation barrier for the reaction are 0.29 ($U = 7$ in the SP system), 0.11 ($U = 4$ in SP system), and 0.65 ($U = 7$ in the NSP system) eV, respectively. Thereafter, the catalytic cycle is completed by desorption of the CO_2, which is an exothermic process releasing energy of 1.74 eV to recover to $Pt_{19}[CO]_{11}$. This proposed reaction pathway is manifested by the MvK mechanism [7]. The simulated reaction pathway using $U = 4$ eV has the same trend with $U = 7$ eV, as shown in figure 4(a). However, the NSP system shows different reaction energy profiles from the SP system. Table 2 summarizes the activation barriers for each system. The major activation barriers (0.47–1.05 eV) of the SP system are apparently close to the measured activation energies ranging from 0.37 to 0.77 eV [36, 83, 85–87], while the NSP system has a much higher barrier (2.19 eV). The elevated barrier in the NSP system is caused by high formation energy of oxygen vacancy, which hampers the release of CO_2 from the surface.

In addition to lowering the activation barrier, the surface spin polarization enables the adsorbed CO on Pt SL to react with O_{surf} to form CO_2. While this reaction is endothermic in the NSP system, the energy released by the reaction is large in the SP system, owing to high surface oxygen reactivity. Compared to the most stable oxygen vacancy on a bare ceria surface, the surface oxygen (at the reaction site marked by red box in figure 4(b)) vacancy formation energy with $Pt_{19}[CO]_{12}$ is lowered by 0.15 eV, thus significantly boosting the reaction with surface oxygen. In figure 4(b), we show the calculated vacancy formation energies for all surface oxygen sites. The interaction between $Pt_{19}[CO]_{12}$ and CeO_2 generally lowers the vacancy formation energies for surface oxygen at exterior sites of the contact zone. However, within the contact zone, the majority of surface oxygen atoms strongly bond with surface Pt (see figure 3(d)). The vacancy formation energies are relatively high for these oxygen, except the oxygen which bonds with Pt–CO (marked by green circle in figure 4(b)). The O_{surf}–Pt–CO at the exceptional site may migrate by forming dynamic low-coordinated atoms, causing a strong dynamic reconfiguration that will be discussed in the following section.

Table 2. The list of activation barriers for the proposed reaction pathway. The major barriers are highlighted in bold.

Calculation type	Parameter	Reaction barrier (eV)		
	U (eV)	TS1	-CO_2	TS2
Spin polarization	7.0	0	**1.05**	0.29
Spin polarization	4.0	0	**0.47**	0.11
Non-spin polarization	7.0	0.82	**2.19**	0.65

3.4. Structural dynamics

The dynamic lattice reconfiguration of nanoparticles upon exposing to oxidizing and reducing gases (e.g. CO and O_2) has been intensively studied by transmission electron microscopy (TEM) in the recent years [34–36, 51, 88–96]. These studies imply that the surface and perimeter of nanoparticle strongly interact with CO and O_2 gases. To explore the influence of surface spin polarization on dynamic lattice reconfiguration, we performed two independent AIMD simulations of ceria-supported Pt nanoparticles with and without the inclusion

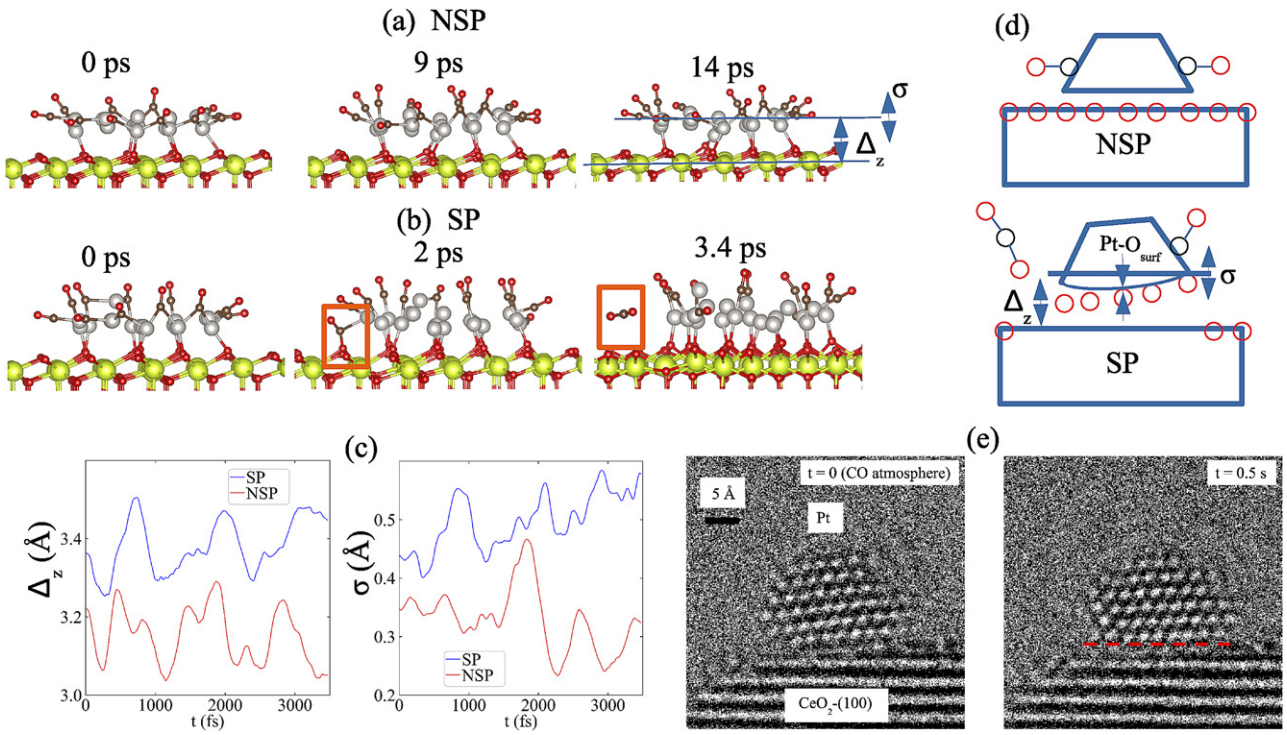

Figure 5. (a) The snapshot of NSP AIMD simulation of the ceria-supported Pt_{19} single layer with 12 CO molecules at 0, 9 and 14 ps. (b) The snap shot of SP AIMD simulation of the ceria-supported Pt_{19} single layer with 12 CO molecules at 0, 2 and 3.4 ps. The red box shows that the CO and surface O bind to form CO_2. (c) Left panel: calculated distance between the average z coordinates of surface Ce atoms and the average z coordinates of Pt atoms, right panel: standard deviation of z coordinates of Pt atoms. (d) Schematic diagram of lattice dynamic in SP and NSP systems. (e) Atomic resolution transmission electron microscope images of fluxional Pt nanoparticle on CeO_2-(100) surface in a CO atmosphere (7×10^{-4} Torr) at room temperature. Pt columns are visible as white dots whereas (100) Miller planes in CeO_2 appear as white horizontal lines. The two images are from the same nanoparticle with right-hand image recorded 0.5 s after the left-hand image.

of spin polarization. Due to the limitation of computational resources, we used only three layers of O–Ce–O.

Despite the artifact due to the choice of a thin CeO_2 slab, our simulations still reveal distinct physical pictures due to the inclusion of spin polarization. In the NSP AIMD simulation (figure 5(a)), the whole system does not show any obvious structural change for 20 ps. On the other hand, we observed rapid CO_2 formation at around 3 ps (figure 5(b)) when the spin polarization is turned on. Figure 5(c) plots the calculated distance between the averaged z coordinates of surface Ce/Pt atoms, as well as the standard deviation to evaluate dispersion of z coordinates of Pt atoms during the simulation. Clearly, the Pt atoms in the SP system are more distant from surface Ce atoms with a larger fluctuation, in comparison to the NSP system. Accordingly, we identify four different features of the SP system (see figure 5(d)). First, strong bonds between Pt and surface oxygen atoms are found in the SP system. This is shown by more bonds and shorter bond lengths because oxygen has moved toward the Pt layer as seen in figure 3. Second, the large distances between surface Ce and Pt atoms are present consistently in the SP AIMD simulations. Highly reducible surface oxygen in the SP surface bond strongly with Pt atoms, resulting in an elevation of surface oxygen and Pt atoms from CeO_2 surface. This shifting is also manifested in the optimized structures in figure 3. Third, substantial fluctuations of Pt atoms are displayed in the SP AIMD simulations, indicating that the elevated Pt nanoparticle from CeO_2 surface are flexible. Fourth, asymmetric CO oxidation was raised by irregular structure of Pt and nonuniform surface O vacancy formation energies as shown in figure 4(b).

Recently, experimental evidence has been published that shows significant lattice reconfiguration on Pt nanoparticles supported on CeO_2 on exposure to CO and other gases [35, 36, 96]. While the timescales for the computation and experimental datasets are very different, precluding a detailed quantitative structural comparison, there is qualitative agreement in the trends in structural dynamics from both theory and experiment. Figure 5(e) is *in situ* electron microscopy data showing dynamic structural change taking place in a CO atmosphere (for experimental details see reference [96]). The Pt nanoparticles undergoes complex lattice changes such as clockwise rotation, uneven Pt atomic plane near the CeO_2, and apparent change on the Pt surface. There are also continuing changes in the interface structure due to the constant creation and annihilation of oxygen vacancies at perimeter sites. This occurs due to the weakening of the interfacial bonds in the presence of CO and the experimental observation can be understood in terms of the schematic diagram of figure 5(d). There are many other fluxional observations such as dynamic changes in cation positions due to breaking and formation of chemical bonds at the perimeter sites which are described in greater detail in the author's paper [36]. These complex dynamics may be described by concerted effect from aforementioned four features, which are pronounced in our

SP AIMD simulation. Thus, we suggest that surface spin polarization may play a deterministic role in promoting the dynamic lattice reconfiguration of ceria-supported Pt nanoparticles.

3.5. Cross-validation of the DFT simulation results

To check if the aforementioned results are robust, we conducted two kinds of validations by considering two important factors (functional and basis set) that can greatly impact the DFT simulation.

In terms of magnetism, appropriate consideration of temperature effect and the nature of strongly correlated electrons is often beyond DFT's assumption. Hence, DFT methods may overestimate or underestimate magnetism due to the choices of functionals. It requires a benchmark test to determine the proper functional (including U) to use based on a comparison with the experimental data. First, we examined the dependence of functionals within the CP2K simulation. When it comes to surface spin polarization on ceria slab, we conducted test simulations using both LDA and PBE functionals. Using LDA, we produced surface spin polarization with ferromagnetic coupling on surface cerium atoms. The calculated spin moment is 0.004 μ_B/Ce in the surface layer. Using PBE, a similar surface spin polarization with a spin moment of 0.79 μ_B/Ce was found. However, unaccounted effect of on-site Coulomb interaction U leads to occupied Ce f band, resulting in a spin polarization located at the middle layer of ceria slab. Upon our examination, we attest that PBE + U and Gaussian type orbitals (GTO) are proper functional and basis by comparing the following properties: (i) the calculated spin moment of ∼0.5 μ_B/Ce in the surface layer, which corresponds to saturation magnetization of 117 kA m^{-1} is within the measured magnetizations range from 91 to 450 kA m^{-1} for 20–30 nm thick CeO_2 films (see table 3 in reference [37]); (ii) our result of surface spin polarization on the pure surface supports for two experiments, which suggests that the ferromagnetism does not relate to the surface oxygen vacancy [55, 59]; (iii), the calculated surface energy of ∼1.0 J m^{-2} is in good agreement with measured surface energy of 1.2 ± 0.2 J m^{-2} [75]; (iv) reasonable oxygen vacancy formation energy less than 0.4 eV support for the consensus that ceria is easily reducible [97, 98]; (v) the simulated activation barrier ∼1.0 eV is close to measured CO oxidation activation energies ranging from 0.37 to 0.73 eV [83, 85–87].

Second, we checked the existence of stable SP configuration using two other DFT codes (VASP [99, 100] and Elk [101]). We conducted fixed spin moments (FSM) calculation using the Elk code with LDA + U (U = 6.8 eV) and 10 × 10 × 1 k-mesh. The total energy of zero fixed spin moment calculation was set as zero. As shown in figure 6(a), the red line is the energy for only surface Ce atoms' spin moments fixed calculation. Clearly, the calculations with FSM on surface Ce or O–Ce–O give rise to increased total energy with respect to constrained magnetic moments. We attribute the absence of stable SP configuration to the choice of basis set in the DFT simulation. To compare the basis-dependent effects, we calculated DOS for three O–Ce–O layers CeO_2 without considering spin polarization. Figure 6(b) shows DOSs for projector augmented wave (PAW) method with plane wave basis, linearised

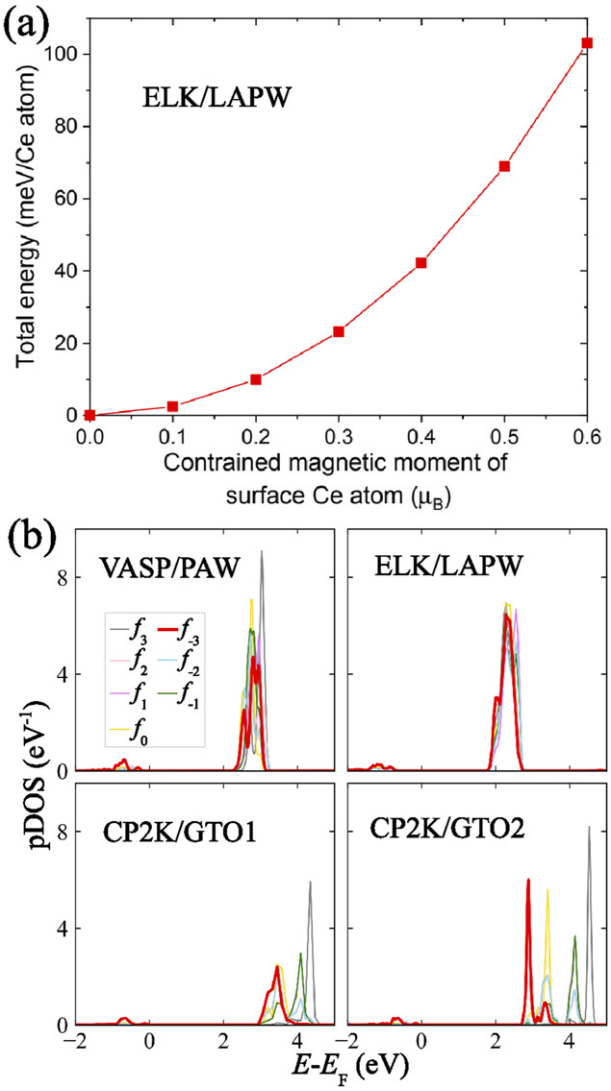

Figure 6. (a) Calculated total energy with respect to constrained magnetic moment for CeO_2 1 × 1 × 6 supercell (six O–Ce–O layers) with 15 Å vacuum. (b) Surface Ce-f projected DOS for three O–Ce–O layers CeO_2 without considering spin polarization for VASP/PAW (left upper), Elk/LAPW (right upper), CP2K/GTO1 (left lower) and CP2K/GTO2 (right lower).

augmented plane wave (LAPW) method with local orbitals, and Gaussian/plane waves approach using GTO. The Ce-f_{-3} orbitals on the surface, which play an important role in the surface charge transfer process, were shown in figure 6(b) as red thick lines. While GTO f_{-3} orbital is split from other f orbitals and is well localized at lower energy, PAW and LAPW f_{-3} orbital coincide with other f orbitals. The f_{-3} localization is more pronounced on DOS for GTO2 than that for GTO1 which is constructed by adding a series of uncontracted Gaussian f functions on GTO2 [102]. We obtained small surface spin polarization of 0.14 and 0.008 μ_B for U = 4 and U = 7 eV, respectively using the uncontracted GTO1. These results indicate that confined GTO2 basis effectively localize the strongly correlated f electron or hole on f_{-3} orbital. It thus promotes charge transfer and enhance exchange interaction by electron localized on just f_{-3} orbital without delocalization on the

others f orbitals, as shown in figure 1(a) for SP system. In this work, we used plane wave basis set with kinetic cutoff energy of 800 eV. We suggest that employing plane wave basis set of much higher kinetic energy may be suitable for the f electron localization. In conclusion, no spin polarization can be found in other DFT simulations based on the PAW or LAPW basis set.

4. Conclusions

In summary, we report the robust surface spin polarization on the CeO_2-(111) surface due to charge transfer from surface oxygen to cerium. According to the CP2K simulation, the surface spin polarization appears to be essential to describe the existing important observations such as ferromagnetism in undoped CeO_2 nanostructures and thin films, high reducibility of ceria support, and low CO oxidation reaction barrier. In addition, the surface spin polarization enhances the bonding between platinum and surface oxygen. However, the presence of surface spin polarization cannot be found with other codes based on different basis set. As such, it will critical to examine it with more advanced approaches such as dynamical mean-field theory (DMFT) [103]. For example, within the LDA + DMFT method, the correct magnetic properties of 2D VSe_2 was calculated, taking into account both itinerant and localized characters of strongly correlated electron [104]. If the spin polarization does exist on the pure ceria surface, it is likely to play an important role in guiding the design of high-performance heterogeneous catalysts.

Acknowledgments

The computing resources are provided by XSEDE (TG-DMR180040). The authors gratefully acknowledge financial support from the National Science Foundation (NSF). BK and QZ are supported by NSF-OAC Award 1940272. NSF-CBET Award 1604971 and NSF-OAC Award 1940263 supported JLV and PAC, who acquired and processed the experimental data and participated in extensive discussion of the calculations. The authors thank Arizona State University's John M Cowley Center for High Resolution Electron Microscopy for microscope access and use. YL and LK are supported by the US Department of Energy, Office of Science, Office of Basic Energy Sciences, Materials Sciences and Engineering Division. Ames Laboratory is operated for the US Department of Energy by Iowa State University under Contract No. DE-AC02-07CH11358.

Data availability statement

The data generated and/or analysed during the current study are not publicly available for legal/ethical reasons but are available from the corresponding author on reasonable request.

ORCID iDs

Qiang Zhu https://orcid.org/0000-0002-9892-0344

References

[1] Stair P C 2011 *Nat. Chem.* **3** 345
[2] Yamada Y, Tsung C K, Huang W, Huo Z, Habas S E, Soejima T, Aliaga C E, Somorjai G A and Yang P 2011 *Nat. Chem.* **3** 372
[3] Zhang J *et al* 2019 *J. Am. Chem. Soc.* **141** 2975
[4] Song S, Wu Y, Ge S, Wang L, Wang Y, Guo Y, Zhan W and Guo Y 2019 *ACS Catal.* **9** 6177
[5] Zhu H, Wu Z, Su D, Veith G M, Lu H, Zhang P, Chai S H and Dai S 2015 *J. Am. Chem. Soc.* **137** 10156
[6] Fang Y *et al* 2020 *ACS Appl. Mater. Interfaces* **12** 7091
[7] Mars P and Van Krevelen D W 1954 *Chem. Eng. Sci.* **3** 41
[8] Tauster S, Fung S and Garten R L 1978 *J. Am. Chem. Soc.* **100** 170
[9] Tauster S, Fung S, Baker R and Horsley J 1981 *Science* **211** 1121
[10] Tauster S 1987 *Acc. Chem. Res.* **20** 389
[11] Tang H *et al* 2017 *Sci. Adv.* **3** e1700231
[12] Wang H, Wang L, Lin D, Feng X, Niu Y, Zhang B and Xiao F S 2021 *Nat. Catal.* **4** 418
[13] Pacchioni G and Freund H J 2018 *Chem. Soc. Rev.* **47** 8474
[14] Campbell C T 2012 *Nat. Chem.* **4** 597
[15] Pacchioni G 2013 *Phys. Chem. Chem. Phys.* **15** 1737
[16] Ro I, Resasco J and Christopher P 2018 *ACS Catal.* **8** 7368
[17] Haruta M 1997 *Catal. Today* **36** 153
[18] Boubnov A, Dahl S, Johnson E, Molina A P, Simonsen S B, Cano F M, Helveg S, Lemus-Yegres L J and Grunwaldt J D 2012 *Appl. Catal. B Environ.* **126** 315
[19] Liu J 2017 *ACS Catal.* **7** 34
[20] Ruiz Puigdollers A, Schlexer P, Tosoni S and Pacchioni G 2017 *ACS Catal.* **7** 6493
[21] Wang Y G, Yoon Y, Glezakou V A, Li J and Rousseau R 2013 *J. Am. Chem. Soc.* **135** 10673
[22] Liu H H, Wang Y, Jia A P, Wang S Y, Luo M F and Lu J Q 2014 *Appl. Surf. Sci.* **314** 725
[23] Liu K, Wang A and Zhang T 2012 *ACS Catal.* **2** 1165
[24] Widmann D and Behm R J 2011 *Angew. Chem., Int. Ed.* **50** 10241
[25] Kim H Y, Lee H M and Henkelman G 2012 *J. Am. Chem. Soc.* **134** 1560
[26] Vayssilov G N *et al* 2011 *Nat. Mater.* **10** 310
[27] Somorjai G A 1991 *Langmuir* **7** 3176
[28] Imbihl R and Ertl G 1995 *Chem. Rev.* **95** 697
[29] Ertl G 2008 *Angew. Chem., Int. Ed.* **47** 3524
[30] Cotton F 1975 *J. Organomet. Chem.* **100** 29
[31] Zhang Z, Zandkarimi B and Alexandrova A N 2020 *Acc. Chem. Res.* **53** 447
[32] Sun G and Sautet P 2018 *J. Am. Chem. Soc.* **140** 2812
[33] Zhai H and Alexandrova A N 2017 *ACS Catal.* **7** 1905–11
[34] Lawrence E L, Levin B D A, Boland T, Chang S L Y and Crozier P A 2021 *ACS Nano* **15** 2624
[35] Li Y *et al* 2021 *Nat. Commun.* **12** 914
[36] Vincent J L and Crozier P A 2021 arXiv:2104.00821
[37] Ackland K and Coey J 2018 *Phys. Rep.* **746** 1
[38] Ni Y, Deng G, Li J, Hua H and Liu N 2021 *ACS Omega* **6** 15308–15
[39] Panneerselvam I R, Chakraborty P, Nian Q, Lu Y, Liao Y and Wang Y 2021 *Semicond. Sci. Technol.* **37** 025013

[40] Jiang X, Wang R, Shelby R M, Macfarlane R M, Bank S R, Harris J S and Parkin S S P 2005 *Phys. Rev. Lett.* **94** 056601
[41] Lin M-W *et al* 2016 *J. Mater. Chem.* C **4** 315
[42] Horváthová L, Derian R, Mitas L and Štich I 2014 *Phys. Rev.* B **90** 115414
[43] He J, Ding G, Zhong C, Li S, Li D and Zhang G 2019 *Nanoscale* **11** 356
[44] Cheng H, Zhou J, Yang M, Shen L, Linghu J, Wu Q, Qian P and Feng Y P 2018 *J. Mater. Chem.* C **6** 8435
[45] Wan Y, Sun Y, Wu X and Yang J 2018 *J. Phys. Chem.* C **122** 989
[46] Artini C, Pani M, Carnasciali M M, Buscaglia M T, Plaisier J R and Costa G A 2015 *Inorg. Chem.* **54** 4126
[47] VandeVondele J, Krack M, Mohamed F, Parrinello M, Chassaing T and Hutter J 2005 *Comput. Phys. Commun.* **167** 103
[48] Goedecker S, Teter M and Hutter J 1996 *Phys. Rev.* B **54** 1703
[49] Perdew J P, Burke K and Ernzerhof M 1996 *Phys. Rev. Lett.* **77** 3865
[50] Grimme S, Antony J, Ehrlich S and Krieg H 2010 *J. Chem. Phys.* **132** 154104
[51] He Y, Liu J C, Luo L, Wang Y G, Zhu J, Du Y, Li J, Mao S X and Wang C 2018 *Proc. Natl Acad. Sci. USA* **115** 7700
[52] Wang Y G, Mei D, Glezakou V A, Li J and Rousseau R 2015 *Nat. Commun.* **6** 6511
[53] Henkelman G, Uberuaga B P and Jónsson H 2000 *J. Chem. Phys.* **113** 9901
[54] Anwar M, Kumar S, Ahmed F, Arshi N, Kil G S, Park D W, Chang J and Koo B H 2011 *Mater. Lett.* **65** 3098
[55] Li M, Ge S, Qiao W, Zhang L, Zuo Y and Yan S 2009 *Appl. Phys. Lett.* **94** 152511
[56] Paunović N, Dohčević-Mitrović Z, Scurtu R, Aškrabić S, Prekajski M, Matović B and Popović Z V 2012 *Nanoscale* **4** 5469
[57] Phokha S, Swatsitang E and Maensiri S 2015 *Electron. Mater. Lett.* **11** 1012
[58] Sundaresan A and Rao C 2009 *Nano Today* **4** 96
[59] Liu Y, Lockman Z, Aziz A and MacManus-Driscoll J 2008 *J. Phys.: Condens. Matter.* **20** 165201
[60] Li M, Zhang R, Zhang H, Feng W and Liu X 2010 *Micro Nano Lett.* **5** 95
[61] Fernandes V *et al* 2010 *Electrochem. Solid-State Lett.* **14** P9
[62] Fernandes V *et al* 2010 *J. Phys.: Condens. Matter.* **22** 216004
[63] Fernandes V *et al* 2009 *Phys. Rev.* B **80** 035202
[64] Li G R, Qu D L, Yu X L and Tong Y X 2008 *Langmuir* **24** 4254
[65] Figueiredo-Prestes N *et al* 2016 *RSC Adv.* **6** 56785
[66] Ge M, Wang H, Liu E, Liu J, Jiang J, Li Y, Xu Z and Li H 2008 *Appl. Phys. Lett.* **93** 062505
[67] El Hachimi A, Zaari H, Boujnah M, Benyoussef A, El Yadari M and El Kenz A 2014 *Comput. Mater. Sci.* **85** 134
[68] Keating P R, Scanlon D O, Morgan B J, Galea N M and Watson G W 2012 *J. Phys. Chem.* C **116** 2443
[69] Ribeiro A N and Ferreira N S 2017 *Phys. Rev.* B **95** 144430
[70] Han X, Amrane N, Zhang Z and Benkraouda M 2016 *J. Phys. Chem.* C **120** 13325
[71] Han X, Lee J and Yoo H I 2009 *Phys. Rev.* B **79** 100403
[72] Ribeiro R A, Andrés J, Longo E and Lazaro S R 2018 *Appl. Surf. Sci.* **452** 463
[73] Hashim A H, Zayed A O H, Zain S M, Lee V S and Said S M 2018 *Appl. Surf. Sci.* **427** 1090
[74] Munoz M C, Gallego S and Sanchez N 2011 *J. Phys.: Conf. Ser.* **303** 012001
[75] Hayun S, Ushakov S V and Navrotsky A 2011 *J. Am. Ceram. Soc.* **94** 3679
[76] Song Y L, Yin L L, Zhang J, Hu P, Gong X Q and Lu G 2013 *Surf. Sci.* **618** 140
[77] Li H Y, Wang H F, Gong X Q, Guo Y L, Guo Y, Lu G and Hu P 2009 *Phys. Rev.* B **79** 193401
[78] Ganduglia-Pirovano M V, Da Silva J L and Sauer J 2009 *Phys. Rev. Lett.* **102** 026101
[79] Han Z K, Yang Y Z, Zhu B, Ganduglia-Pirovano M V and Gao Y 2018 *Phys. Rev. Mater.* **2** 035802
[80] Chen F, Liu D, Zhang J, Hu P, Gong X Q and Lu G 2012 *Phys. Chem. Chem. Phys.* **14** 16573
[81] Huang M and Fabris S 2008 *J. Phys. Chem.* C **112** 8643
[82] Nolan M and Watson G W 2006 *J. Phys. Chem.* B **110** 16600
[83] Lu Y, Thompson C, Kunwar D, Datye A K and Karim A M 2020 *ChemCatChem* **12** 1726
[84] Das S, Dutta K, Shul Y G and Kundu P P 2015 *Crit. Rev. Solid State Mater. Sci.* **40** 316
[85] Ke J *et al* 2015 *ACS Catal.* **5** 5164
[86] Cargnello M, Doan-Nguyen V V, Gordon T R, Diaz R E, Stach E A, Gorte R J, Fornasiero P and Murray C B 2013 *Science* **341** 771
[87] Kopelent R, van Bokhoven J A, Szlachetko J, Edebeli J, Paun C, Nachtegaal M and Safonova O V 2015 *Angew. Chem.* **127** 8852
[88] Hansen P L, Wagner J B, Helveg S, Rostrup-Nielsen J R, Clausen B S and Topsøe H 2002 *Science* **295** 2053
[89] Nagai Y *et al* 2008 *Angew. Chem., Int. Ed.* **47** 9303
[90] Vendelbo S B *et al* 2014 *Nat. Mater.* **13** 884
[91] Gänzler A M, Casapu M, Boubnov A, Müller O, Conrad S, Lichtenberg H, Frahm R and Grunwaldt J D 2015 *J. Catal.* **328** 216
[92] Gänzler A M, Casapu M, Vernoux P, Loridant S, Cadete Santos Aires F J, Epicier T, Betz B, Hoyer R and Grunwaldt J D 2017 *Angew. Chem., Int. Ed.* **56** 13078
[93] Lawrence E L and Crozier P A 2018 *ACS Appl. Nano Mater.* **1** 1360
[94] Miller B K and Crozier P A 2021 *ACS Catal.* **11** 1456
[95] Tao F and Crozier P A 2016 *Chem. Rev.* **116** 3487
[96] Vincent J and Crozier P 2020 *Microsc. Microanal.* **26** 1694
[97] Mullins D R 2015 *Surf. Sci. Rep.* **70** 42
[98] Song X Z, Zhu W Y, Wang X F and Tan Z 2021 *ChemElectroChem* **8** 996
[99] Kresse G and Hafner J 1994 *Phys. Rev.* B **49** 14251
[100] Kresse G and Furthmüller J 1996 *Phys. Rev.* B **54** 11169
[101] The Elk code http://elk.sourceforge.net/
[102] Wang Y G, Mei D, Li J and Rousseau R 2013 *J. Phys. Chem.* C **117** 23082
[103] Georges A, Kotliar G, Krauth W and Rozenberg M J 1996 *Rev. Mod. Phys.* **68** 13
[104] Kim T J, Ryee S, Han M J and Choi S 2020 *2D Mater.* **7** 035023